

Data driven learning to enhance a kinetic model of distressed crowd dynamics

November 21, 2024

Daewa Kim

Department of Mathematical Sciences, University of Delaware, 501 Ewing Hall Newark, DE 19716, USA
daewakim@udel.edu

Demetrio Labate, Kamrun Mily, and Annalisa Quaini

Department of Mathematics, University of Houston, 3551 Cullen Blvd, Houston TX 77204, USA
dlabate2@central.uh.edu, kmily@cougarnet.uh.edu, aquaini@central.uh.edu

Abstract

The mathematical modeling of crowds is complicated by the fact that crowds possess the behavioral ability to develop and adapt moving strategies in response to the context. For example, in emergency situations, people tend to alter their walking strategy in response to fear. To be able to simulate these situations, we consider a kinetic model of crowd dynamics that features the level of stress as a parameter and propose to estimate this key parameter by solving an inverse crowd dynamics problem. This paper states the mathematical problem and presents a method for its numerical solution. We show some preliminary results based on a synthetic data set, i.e., test cases where the exact stress level is known and the crowd density data are generated numerically by solving a forward crowd dynamics problem.

Keywords: Crowd dynamics; Boltzmann-type kinetic model; Complex systems; Inverse problems; Parameter estimation.

AMS Subject Classification: 35Q91, 65M08, 91C99

1 Introduction

Stampede-related injuries and deaths continue to happen at events like concerts and religious, festive, or sport gatherings. See Fig. 1 for an example captured on security cameras. Since experiments



Figure 1: Security camera frames of a surge in the crowd gathered in Torino (Italy) to watch a soccer game on June 3rd, 2017. The stampede led to 3 people dead and over 1600 injured. Video available at <https://youtu.be/yuqcNgcgzIA?feature=shared>.

on panicked people are unethical and potentially harmful, the most practical and effective way to improve crowd management is via modeling and computational simulations.

Unlike inert matter, crowds possess the behavioral ability to develop and adapt moving strategies in response to the context, which significantly complicates their mathematical modeling. See Refs. 11, 12 for recent reviews on the topic. A consequence of this complication is that, although the mathematical modeling of crowd motion has fascinated researchers since the 1950s, the large majority of existing mathematical models assume that pedestrians do not alter their, typically rational, walking behavior. However, in emergency situations, people may behave irrationally in response to fear. Thus, an accurate model of crowd dynamics in stressful situations cannot be fully captured by classical mechanics and must include heterogeneous behavior of individual entities and their interactions, accounting for the effects of the individuals' levels of stress and its propagation.^{7,17,19,20,32} While the widely used agent-based models^{18,27,30,33,35} successfully account for heterogeneous individual behavior (each agent can develop a specific walking strategy), they fail to reproduce non-local and nonlinearly additive interactions, becoming progressively less accurate as the number of individuals increases. Thus, in this paper we focus on an alternative model that can reproduce such complex interactions.

Taking inspiration from the kinetic theory of gases, kinetic models of crowd dynamics derive a Boltzmann-type evolution equation for the statistical distribution function of the position and velocity of the pedestrians. In these models, people are seen as *active* particles, as opposed to classical particles in gases. This leads to a key difference: the interactions in kinetic models for gas dynamics are conservative and reversible, while the interactions in the kinetic models for crowd dynamics are irreversible, non-conservative and, in some cases, nonlocal and nonlinearly additive. Hence, kinetic models can overcome the limitations of agents-based models in terms of complexity of interactions. An important consequence of the aforementioned difference is that often for active particles the Maxwellian equilibrium does not exist.² The reader interested in introductory concepts on the kinetic theory of active particles is referred to Refs. 6 and 4. More recent developments

can be found in Refs. 5, 8, 9 and 23. Refs. 11, 12 focus on aspects specific to the modeling of crowds taking into account behavioral dynamics. A recent interesting spin on kinetic models as possible mathematical models for artificial intelligence, i.e., collective behavior of artificial (instead of natural) self-organizing systems, is discussed in Ref. 10.

The kinetic model considered in this paper was initially proposed in⁶ and further developed in^{1,8,23}. It assumes discrete walking directions, a continuous deterministic walking speed, and it accounts for the presence of walls and other kinds of obstacles in the walking domain. The kinetic models in^{1,6,8,23} features the level of stress as a parameter, that in the numerical experiment is set to be constant in space and time. This homogeneity of the stress level in a crowd is obviously not realistic. Hence, some models have introduced the emotional state as a variable that, in response to interactions with other people, can change in space and time and, in turn, alter the walking strategy^{9,14}. In fact, it is known that emotional contagion significantly affects the overall crowd dynamics in complicated real-life situations such as emergency evacuations¹⁷. A multiscale (from agent-based to continuum) approach to crowd dynamics with emotional contagion is introduced in³¹. Therein, the stress level is propagated by a Bhatnagar–Gross–Krook-like model and results are limited to one space dimension. Extension to 2D is presented in²². While treating the emotional state as a variable leads to more realistic simulation results than representing it as a constant parameter⁹, the computational cost of an additional variable can become significant as the domain size increases.

Since the overall goal of crowd dynamics simulations is to contribute to crowd management in emergency situations³, the computational cost of realistic simulations must be contained. Thus, in this paper we propose a third alternative to treat the emotional state. The computational cost is contained by considering the emotional state, i.e., the stress level, as a parameter that is optimized in space and time to match density data extracted from video frames for realism. With a large database of videos such as the one in Fig. 1, one could split the database into validation and training datasets and use the videos in the training set to learn the evolution of the stress level via an optimization procedure that minimizes the difference between the density data extracted from the video and the simulated crowd density. In this paper, we present a possible optimization approach for this purpose. Parameter learning techniques have been proposed for agent-based models.^{13,25,34} However, to the best of our knowledge, it is the first time that such a technique is proposed for a kinetic model.

Extracting crowd density data from security camera footage is challenging due to poor resolution and, typically, reduced visibility. Since these are challenges related to the extraction of data from images and not to the learning-from-data technique, in this paper we considered a simplified setting: videos of experiments where a few hundred ants are enclosed in a simple chamber and an insect repellent is injected at the opposite end of the exit to induce panic.²⁹ Despite the obvious differences between ants and human crowds, these experiments exhibit complex interactions which are comparable to those observed in a human crowd responding to stress or panic.²⁵ In the recorded experiments, the geometric setting is simple: a circular or square chamber with one exit and, in some cases, a column obstructing the exit. Fig. 2 shows the circular chamber with and without

obstructing column. It is clear that the image quality of the frames in Fig. 2 is superior when compared to Fig. 1.

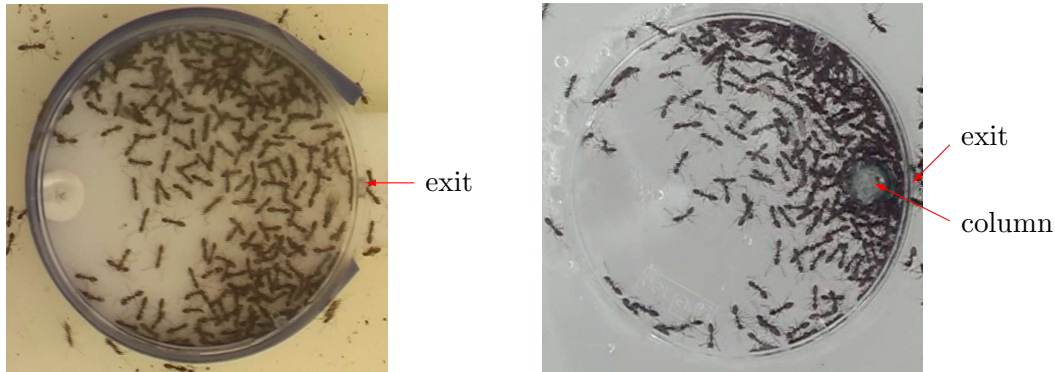


Figure 2: Snapshots of experiments with panicking ants from Ref. 29: circular chamber without (left) and with (right) column obstructing the exit.

There exist several methodologies to estimate the crowd density from images or video frames, including classical methods relying on texture analysis²⁶ and a multiplicity of more recent strategies based on deep learning architectures^{15,16,21}. In this work, we assume that such estimated crowd density, denoted by ρ_v , is available and we minimize the difference between ρ_v and the crowd density computed by our kinetic model, which depends on the stress level parameter. This minimization problem yields an estimation of the stress level, so it can be considered an inverse problem. In fact, inverse problems can be used for parameter identification of mathematical models, also called forward problems, whose state variables are observed through available data. In our case, the forward problem is our kinetic model for crowd dynamics, the state variables are the probability distribution functions, from which crowd density can be computed, and the observed data are the crowd densities extracted from video images. In this paper, we solve the inverse problem as a constrained optimization problem, where the kinetic model is the constraint and the functional to be minimized is a measure of the mismatch between the density data and the computed density solution.

In our approach to the constrained minimization problem, the kinetic model is first discretized in time and then the optimization step is performed. We present a numerical method for its solution. In this first work, we consider the simple geometrical settings used in the experiments on ants²⁹ and synthetic data, i.e., obtained by a forward crowd dynamics problem. The comparison with real data extracted from the videos of the ants experiments, generously shared with us by the authors of Ref. 29, will be presented in a follow-up paper.

The rest of the paper is structured as follows. Sec. 2.1 presents the time continuous inverse crowd dynamics problem and Sec. 3 describes its time discrete counterpart. Numerical methods for the solution are presented in Sec. 4, while numerical results are presented and discussed in Sec. 5.

Sec. 6 draws the conclusions and mentions possible future perspectives.

2 The time continuous inverse crowd dynamics problem

2.1 The forward problem

Let $\Omega \subset \mathbb{R}^2$ denote a bounded walkable domain. We assume that the boundary $\partial\Omega$ includes an exit E , which could be the finite union of disjoint sets, and walls W . Here, $\overline{E} \cup \overline{W} = \overline{\partial\Omega}$ and $E \cap W = \emptyset$. Let $\mathbf{x} = (x, y) \in \Omega$ denote position and $\mathbf{v} = v(\cos \theta, \sin \theta) \in \Omega_{\mathbf{v}}$ denote velocity, where v is the velocity modulus, θ is the velocity direction, and $\Omega_{\mathbf{v}} \subset \mathbb{R}^2$ is the velocity domain. For a system composed by a large number of people distributed inside Ω , the distribution function is given by

$$f = f(t, \mathbf{x}, \mathbf{v}) \quad \text{for all } t \geq 0, \mathbf{x} \in \Omega, \mathbf{v} \in \Omega_{\mathbf{v}}.$$

Since we use polar coordinates for the velocity, we can write the distribution function as $f = f(t, \mathbf{x}, v, \theta)$, where v is the walking speed and θ is the walking direction. Under suitable integrability conditions, $f(t, \mathbf{x}, v, \theta) d\mathbf{x} dv$ represents the number of individuals who, at time t , are located in the infinitesimal rectangle $[x, x+dx] \times [y, y+dy]$ and have a velocity belonging to $[v, v+dv] \times [\theta, \theta+d\theta]$.

For simplicity, we assume θ can take values in the set:

$$I_{\theta} = \left\{ \theta_i = \frac{i-1}{N_d} 2\pi : i = 1, \dots, N_d \right\},$$

where N_d is the maximum number of possible directions. The scale of observation for a kinetic model can be considered between the scale of agent-based models (i.e., microscopic) and the scale of continuum models (i.e., macroscopic). Hence, the assumption of discrete walking directions is reasonable because if there was a large enough crowd in every possible walking direction then a macroscopic model would be more suited. To further simplify the problem, we model the walking speed v as a continuous deterministic variable that evolves in time and space depending on the crowd density. This is also a reasonable assumption since the walking speed of a person typically depends on the level of congestion around them.

Since v is now a deterministic variable, we can reduce the distribution function to

$$f(t, \mathbf{x}, \theta) = \sum_{i=1}^{N_d} f^i(t, \mathbf{x}) \delta(\theta - \theta_i), \quad (2.1)$$

where $f^i(t, \mathbf{x}) = f(t, \mathbf{x}, \theta_i)$ is related to the number of individuals that, at time t and position \mathbf{x} , walk with direction θ_i . In equation (2.1), δ denotes the Dirac delta function.

From now on, we will assume that all variables are dimensionless. See, e.g., Ref. 23 for details on how the non-dimensionalization process is carried out. Due to the normalization of f and each

f^i , the dimensionless local density is obtained by summing the distribution functions over the set of directions:

$$\rho(t, \mathbf{x}) = \sum_{i=1}^{N_d} f^i(t, \mathbf{x}). \quad (2.2)$$

As mentioned above, the walking speed is a function of ρ in (2.2). For simplicity, we assume that the quality of the walkable domain is high everywhere, meaning that a person can walk at the maximum dimensionless speed (i.e., 1) everywhere in Ω . This maximum walking speed can be kept so long as the density around a person does not reach a critical value ρ_c , past which the person is forced to slow down. Following experimental estimates published in the literature,²⁸ we set $\rho_c = 1/5$. In the slowdown zone, i.e., for $\rho > \rho_c$, we assume the walking speed is a cubic polynomial in ρ . See, e.g., Ref. 23 for the exact definition. Figure 3 reports v as a function of ρ .

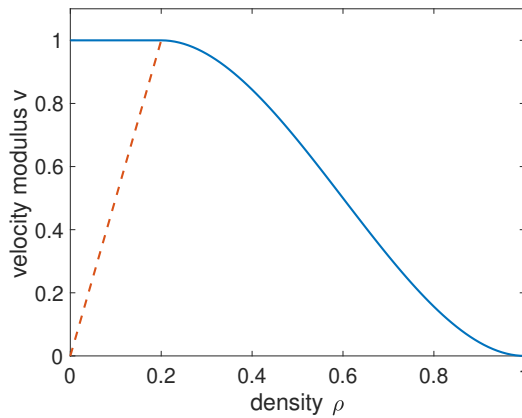


Figure 3: Dependence of the dimensionless velocity modulus v on the dimensionless density ρ . The dashed red line connects the origin of the axis to the critical value $\rho_c = 1/5$.

Remark 2.1 The assumption of high quality of the walkable domain is reasonable for the experiments on ants, but it would make perhaps less sense in a real life context such as the one in Fig. 1. An easy way to incorporate the quality of the domain in the model is through a parameter. The reader interested in this is referred to, e.g., Refs. 11, 12.

A model governing the dynamics of a crowd can be obtained by a balance of people, or active particles, in an elementary volume of the space of microscopic states, considering the net flow into such a volume due to transport and interactions with other people and the environment:

$$\frac{\partial f^i}{\partial t} + \nabla \cdot (\mathbf{v}[\rho](t, \mathbf{x}) f^i(t, \mathbf{x})) = \mathcal{I}^i[f](t, \mathbf{x}) \quad (2.3)$$

for $i = 1, 2, \dots, N_d$. By $[\cdot]$, we mean nonlinear dependence on the argument. Functional $\mathcal{I}^i[f]$ represents the net balance of people that walk with direction θ_i . One way to look at $\mathcal{I}^i[f]$ could be as follows:

$$\mathcal{I}^i[f] = \mathcal{G}^i[f] - \mathcal{L}^i[f],$$

where \mathcal{G} and \mathcal{L} represent gain and loss, both acting nonlinearly on f , of people walking with direction θ^i in the elementary volume. However, for our purpose, it is more convenient to write $\mathcal{I}^i[f]$ as:

$$\mathcal{I}^i[f](t, \mathbf{x}) = \mathcal{I}_G^i[f](t, \mathbf{x}) + \mathcal{I}_P^i[f](t, \mathbf{x}),$$

where \mathcal{I}_G^i is an interaction between *candidate* people and the environment, and \mathcal{I}_P^i is an interaction between *candidate* and *field* people. This terminology is borrowed from gas dynamics: a *test* individual i is representative of the whole system, and a *candidate* individual h reaches in probability the state of the test individual after interactions with the environment or with *field* people.

We define \mathcal{I}_G^i and \mathcal{I}_P^i as

$$\begin{aligned} \mathcal{I}_G^i[f](t, \mathbf{x}) &= (1 - \rho) \left(\sum_{h=1}^{N_d} \mathcal{A}_h^i f^h(t, \mathbf{x}) - f^i(t, \mathbf{x}) \right), \\ \mathcal{I}_P^i[f](t, \mathbf{x}) &= \rho \left(\sum_{h,k=1}^{N_d} \mathcal{B}_{hk}^i[\rho] f^h(t, \mathbf{x}) f^k(t, \mathbf{x}) - f^i(t, \mathbf{x}) \rho \right), \end{aligned}$$

where

- \mathcal{A}_h^i is the probability that a candidate individual h , i.e. with direction θ_h , adjusts their direction into that of the test individual θ_i due to the presence of walls, obstacles and/or an exit. The following constraint for \mathcal{A}_h^i has to be satisfied:

$$\sum_{i=1}^{N_d} \mathcal{A}_h^i = 1 \quad \text{for all } h \in \{1, \dots, N_d\}.$$

- \mathcal{B}_{hk}^i is the probability that a candidate individual h modifies their direction θ_h into that of the test individual i , i.e., θ_i , due to the interaction with a field individual k that moves with direction θ_k . The following constraint for \mathcal{B}_{hk}^i has to be satisfied:

$$\sum_{i=1}^{N_d} \mathcal{B}_{hk}^i = 1 \quad \text{for all } h, k \in \{1, \dots, N_d\}. \quad (2.4)$$

The transition probabilities \mathcal{A}_h^i and \mathcal{B}_{hk}^i are meant to account for the process through which a person decides the direction to take. Let us start from defining \mathcal{A}_h , which accounts for the following two factors in deciding the walking direction:

- *The goal to reach the exit.*

Given a candidate individual at point \mathbf{x} , we define their distance to the exit as

$$d_E(\mathbf{x}) = \min_{\mathbf{x}_E \in E} \|\mathbf{x} - \mathbf{x}_E\|,$$

and we consider the unit vector $\mathbf{u}_E(\mathbf{x})$, pointing from \mathbf{x} to the exit. See Figure 4.

- *The desire to avoid collisions with the walls.*

Given a candidate individual at the point \mathbf{x} walking with direction θ_h , we define the distance $d_W(\mathbf{x}, \theta_h)$ from the individual to a wall at a point $\mathbf{x}_W(\mathbf{x}, \theta_h)$, where the person is expected to collide with the wall. The unit tangent vector $\mathbf{u}_W(\mathbf{x}, \theta_h)$ to $\partial\Omega$ at \mathbf{x}_W points to the direction of the the exit. Vector \mathbf{u}_W is used to avoid a collision with the wall. See Figure 4.

Let θ_G be the *geometrical preferred direction*, which accounts for the above two factors:

$$\begin{aligned} \mathbf{u}_G(\mathbf{x}, \theta_h) &= \frac{(1 - d_E(\mathbf{x}))\mathbf{u}_E(\mathbf{x}) + (1 - d_W(\mathbf{x}, \theta_h))\mathbf{u}_W(\mathbf{x}, \theta_h)}{\|(1 - d_E(\mathbf{x}))\mathbf{u}_E(\mathbf{x}) + (1 - d_W(\mathbf{x}, \theta_h))\mathbf{u}_W(\mathbf{x}, \theta_h)\|} \\ &= (\cos \theta_G, \sin \theta_G). \end{aligned} \quad (2.5)$$

A candidate individual h will update their direction by choosing the angle closest to θ_G . Then, we define \mathcal{A}_h^i as:

$$\mathcal{A}_h^i = \begin{cases} 1 - \frac{4}{\pi}|\theta_G - \theta_i| & \text{if } |\theta_G - \theta_i| \leq \frac{\pi}{4}, \\ 0 & \text{if } |\theta_G - \theta_i| > \frac{\pi}{4}, \end{cases} \quad (2.6)$$

with

$$d(\theta_p, \theta_q) = \begin{cases} |\theta_p - \theta_q| & \text{if } |\theta_p - \theta_q| \leq \pi, \\ 2\pi - |\theta_p - \theta_q| & \text{if } |\theta_p - \theta_q| > \pi. \end{cases} \quad (2.7)$$

Transition probability \mathcal{B}_{hk}^i accounts for the following factors in deciding the walking direction:

- *The tendency to look for less congested areas.*

A candidate person (\mathbf{x}, θ_h) may decide to change direction in order to avoid congested areas. One way to do this is by considering the minimal directional derivative of the density at the point \mathbf{x} . We denote such a direction by unit vector $\mathbf{u}_C(\theta_h, \rho) = (\cos \theta_C, \sin \theta_C)$, with

$$C = \arg \min_{j \in \{h-1, h, h+1\}} \{\partial_j \rho(t, \mathbf{x})\}.$$

In conditions of no-stress, people typically choose this walking strategy.

- *The tendency to follow the stream.*

A candidate person h interacting with a field person k may decide to follow the field person and thus walk with their direction, denoted with unit vector $\mathbf{u}_F = (\cos \theta_k, \sin \theta_k)$. Following the stream is what people tend to do in stressful conditions, like in an emergency evacuation, and is a competing walking strategy to the search for less congested areas.

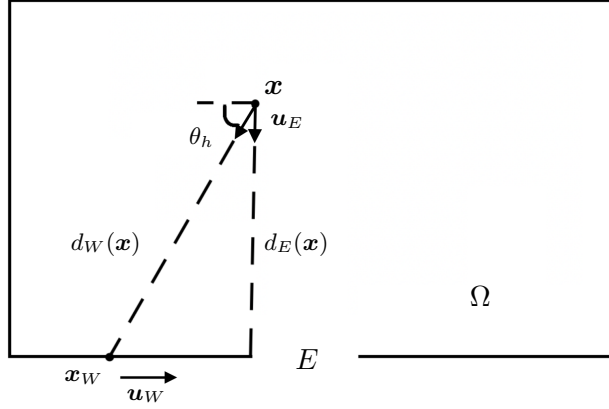


Figure 4: Sketch of computational domain Ω with exit E and a person located at \mathbf{x} , walking with direction θ_h . The person should choose direction \mathbf{u}_E to reach the exit and direction \mathbf{u}_W is to avoid collision with the wall. The person's distances from the exit and from the wall where they would collide are d_E and d_W , respectively.

To weight between these two walking strategies, we introduce a parameter $\varepsilon \in [0, 1]$: $\varepsilon = 0$ corresponds to searching for less congested areas only, while $\varepsilon = 1$ corresponds to only following the stream. Then, the *interaction-based preferred direction* is given by:

$$\mathbf{u}_P(\theta_h, \theta_k, \rho) = \frac{\varepsilon \mathbf{u}_F + (1 - \varepsilon) \mathbf{u}_C(\theta_h, \rho)}{\|\varepsilon \mathbf{u}_F + (1 - \varepsilon) \mathbf{u}_C(\theta_h, \rho)\|} = (\cos \theta_P, \sin \theta_P),$$

and

$$\mathcal{B}_{hk}^i = \begin{cases} 1 - \frac{4}{\pi} |\theta_P - \theta_i| & \text{if } |\theta_P - \theta_i| \leq \frac{\pi}{4}, \\ 0 & \text{if } |\theta_P - \theta_i| > \frac{\pi}{4}. \end{cases} \quad (2.8)$$

We recall that $d(\cdot, \cdot)$ is defined in (2.7). Since $\theta_P - \theta_i = \arccos(\mathbf{u}_P \cdot \mathbf{u}_i)$, (2.8) can be easily computed from:

$$\mathcal{B}_{hk}^i = \begin{cases} 1 - \frac{4}{\pi} |\arccos(\mathbf{u}_P \cdot \mathbf{u}_i)| & \text{if } |\arccos(\mathbf{u}_P \cdot \mathbf{u}_i)| \leq \frac{\pi}{4}, \\ 0 & \text{otherwise,} \end{cases} \quad (2.9)$$

where

$$\mathbf{u}_P \cdot \mathbf{u}_i = \frac{\varepsilon \mathbf{u}_F \cdot \mathbf{u}_i + (1 - \varepsilon) \mathbf{u}_C \cdot \mathbf{u}_i}{\sqrt{\varepsilon^2 + (1 - \varepsilon)^2 + 2\varepsilon(1 - \varepsilon) \mathbf{u}_F \cdot \mathbf{u}_C}}.$$

So, (2.8) is piecewise differentiable in ε .

Remark 2.2 We define \mathcal{A}_h^i and \mathcal{B}_{hk}^i differently from, e.g., Refs. 1, 8, 23. The change is dictated by the need for \mathcal{B}_{hk}^i to be piecewise differentiable for the approach presented in Sec. 3.2. Then, the definition of \mathcal{A}_h^i is changed accordingly. The main difference between our definitions in (2.6)

and (2.8) and those in the above-mentioned references is that we allow people to switch their walking direction to the closest to the geometrical preferred direction, in the case of \mathcal{A}_h^i , or the interaction-based preferred direction, in the case of \mathcal{B}_{hk}^i , while previously the change in direction for the candidate individual h was restricted to $\theta_{h-1}, \theta_h, \theta_{h+1}$.

Finally, let us introduce notation to write model (2.3) in compact form. Let $\mathbf{f} \in \mathbb{R}^{N_d}$ be the vector function whose i -th entry is f^i , $\mathcal{A} \in \mathbb{R}^{N_d \times N_d}$ the matrix whose ih entry is \mathcal{A}_h^i , $\mathcal{B}^i \in \mathbb{R}^{N_d \times N_d}$ the matrix whose hk entry is \mathcal{B}_{hk}^i , and $\mathbf{b} \in \mathbb{R}^{N_d}$ the vector function whose i -th entry is $\mathbf{f}^T \mathcal{B}^i \mathbf{f}$. Furthermore, we define $\mathbf{J} = \mathbf{v} \otimes \mathbf{f}$. Then, model (2.3) can be written in vector form as follows:

$$\frac{\partial \mathbf{f}}{\partial t} + \nabla \cdot \mathbf{J} = (1 - \rho)(\mathcal{A}\mathbf{f} - \mathbf{f}) + \rho(\mathbf{b} - \rho\mathbf{f}). \quad (2.10)$$

2.2 The time-continuous inverse problem

Let us assume that we can extract the density data from the video frames every τ_k , $k = 1, \dots, N$, within the time interval of interest $[0, T]$, where $t = 0$ is the time when the insect repellent is injected, and $T = \tau_N$. In addition, we assume that the time step $\Delta\tau$ to acquire the data is constant. Although simplifying, this assumption is neither unrealistic nor restrictive. We denote by $\rho_v(\tau_k, \mathbf{x})$ the density extracted from the video footage at time τ_k for $\mathbf{x} \in \Omega$.

We introduce the following functional:

$$\mathcal{J}_c = \frac{1}{2} \sum_{k=1}^N \int_{\Omega} (\rho(\tau_k, \mathbf{x}) - \rho_v(\tau_k, \mathbf{x}))^2 d\mathbf{x}, \quad (2.11)$$

where $\rho(\tau_k, \mathbf{x})$ is computed with (2.2) from the solution of (2.10). Usually, a regularization term is added to functional \mathcal{J}_c :

$$\mathcal{J}_c^{\mathcal{R}} = \mathcal{J}_c + \mathcal{R}_c(\varepsilon), \quad (2.12)$$

where \mathcal{R}_c could be Tikhonov regularization, which is expected to improve the mathematical and numerical properties of the minimization process. It could be defined as:

$$\mathcal{R}_c(\varepsilon) = \frac{\xi}{2} \sum_{k=1}^N \int_{\Omega} (\varepsilon(\tau_k, \mathbf{x}) - \varepsilon_{ref}(\tau_k, \mathbf{x}))^2 d\mathbf{x}, \quad (2.13)$$

where ε_{ref} is a reference distribution of the stress level. With this choice of regularization, we are forcing ε to be close to ε_{ref} . Parameter ξ , which weights the importance of the regularization term in the minimization procedure, can be tuned empirically.

Let \mathcal{E} be an admissible set for the control variable ε . We define it as

$$\mathcal{E} = \{\varepsilon : \varepsilon \in L^\infty(\Omega), 0 \leq \varepsilon \leq 1\}. \quad (2.14)$$

Then, we can define the inverse crowd dynamics problem:

Time-continuous problem: For $\mathbf{x} \in \Omega$, find $\varepsilon = \varepsilon(t, \mathbf{x}) \in \mathcal{E}$ that minimizes functional $\mathcal{J}_c^{\mathcal{R}}$ (2.12) under constraints (2.2), (2.10).

This is a time-dependent minimization problem. A possible approach for its solution is the introduction of a Lagrange multiplier for the constraint given by (2.10) and a Lagrangian functional to be minimized with no constraint. Then, the Lagrangian functional is differentiated with respect to the state variable \mathbf{f} , the Lagrange multiplier, and the control variable ε to obtain the classical Karush–Kuhn–Tucker (KKT) system, i.e., state problem, adjoint problem, and optimality condition.

While feasible, this approach has two important drawbacks, both related to the fact that the adjoint of an initial value problem is a final value problem. The first is complexity because the solution of a final value problem is nontrivial. The second is the need to store the solution at all the time steps due to the back-in-time nature of the adjoint problem. Since we prefer to avoid these drawbacks, we follow an alternative approach: we first discretize in time and then minimize the time-discrete problem. The time-discrete problem is presented in Sec. 3.1 and the new minimization problem that arises from this *discretize-then-optimize* approach is stated in Sec. 3.2.

3 The time discrete inverse crowd dynamics problem

3.1 The time discrete forward problem

Let Δt be a constant time step. It is reasonable to assume that $\Delta\tau$, i.e., the time step used to extract the data from the video (see Sec. 2.2), is larger than Δt , which might have to fulfill stability and accuracy requirements. We assume that $\Delta\tau$ is a multiple m of Δt , i.e. $\Delta\tau = m\Delta t$. Should this assumption not hold true, suitable interpolation procedures can be used to interpolate the data at the time discretization nodes. For simplicity of exposition, from now on we will assume that $m = 1$. The case of $m > 1$ would not require a fundamental change in the procedure presented below.

We set $t^n = n\Delta t$, $n = 0, \dots, N$ with $N\Delta t = T$. We denote by y^n the approximation of a generic time-dependent function y at time t^n . For the time discretization of problem (2.10), we consider an explicit method. Although a CFL condition needs to be satisfied for stability, we choose this method for its simplicity and to build upon our previous work,^{22–24} which uses this method. Of course, the approach presented below can be adapted to other time-discretization schemes.

Problem (2.10) discretized in time with a first order explicit method reads: at time t^{n+1} , with $n = 0, \dots, N - 1$, given \mathbf{f}^n , find \mathbf{f}^{n+1} such that

$$\begin{aligned} \frac{\mathbf{f}^{n+1}}{\Delta t} - \rho^n \mathbf{b}(\mathbf{f}^n, \varepsilon^{n+1}) &= \mathbf{g}^n \\ \mathbf{g}^n &= \frac{\mathbf{f}^n}{\Delta t} - \nabla \cdot \mathbf{J}^n + (1 - \rho^n)(\mathcal{A}\mathbf{f}^n - \mathbf{f}^n) - (\rho^n)^2 \mathbf{f}^n, \end{aligned} \tag{3.1}$$

where $\mathbf{b}(\mathbf{f}^n, \varepsilon^{n+1})$ is the vector whose i -th entry is $(\mathbf{f}^n)^T \mathcal{B}^i(\varepsilon^{n+1}) \mathbf{f}^n$ and $\mathbf{J}^n = \mathbf{v}^n \otimes \mathbf{f}^n$. Notice that we have made explicit the dependence of vector \mathbf{b} on \mathbf{f}^n , i.e., the probability distribution function at the previous time step, and ε^{n+1} , i.e., the fear level (our control variable) at the current time step. The right-hand-side in (3.1) depends only on quantities computed at the previous time step. Once \mathbf{f}^{n+1} is obtained from (3.1), the density at time t^{n+1} is found by summing the components of \mathbf{f}^{n+1} :

$$\rho^{n+1} = \sum_{i=1}^{N_d} f^{i,n+1}. \quad (3.2)$$

3.2 The time discrete inverse problem and the KKT conditions

Let us consider functional:

$$\mathcal{J}^n = \frac{1}{2} \int_{\Omega} (\rho(t^n, \mathbf{x}) - \rho_v(t^n, \mathbf{x}))^2 d\mathbf{x}. \quad (3.3)$$

As mentioned in Sec. 2.2, it is typical to add a regularization term \mathcal{R} . If one has chosen regularization (2.13), it could be defined as follows for functional (3.3):

$$\mathcal{R}^n(\varepsilon) = \frac{\xi}{2} \int_{\Omega} (\varepsilon(t^n, \mathbf{x}) - \varepsilon_{ref}(t^n, \mathbf{x}))^2 d\mathbf{x}. \quad (3.4)$$

Then, at every time t^{n+1} , for $n = 0, \dots, N-1$, we have to solve the following new minimization problem:

Time-discrete variational problem: Find $\varepsilon \in \mathcal{E}$ that minimizes functional

$$\mathcal{J}^{\mathcal{R},n+1} = \mathcal{J}^{n+1} + \mathcal{R}^{n+1}(\varepsilon), \quad (3.5)$$

under constraints (3.1)-(3.2).

To find the minimizer of (3.4) under constraints (3.1)-(3.2), we adopt the classical Lagrange multiplier approach. In this method, the problem of finding the minimizer of a functional subject to one or more constraints is reformulated as a saddle point problem. The solution corresponding to the original constrained minimization problem is a saddle point of the so-called Lagrangian functional. For problem (3.4), the Lagrangian functional is given by:

$$\mathcal{L}(\mathbf{F}, \mathbf{\Lambda}, E) = \mathcal{J}^{n+1} + \mathcal{R}^{n+1}(E) + \left\langle \frac{\mathbf{F}}{\Delta t} - \rho^n \mathbf{b}(\mathbf{f}^n, E) - \mathbf{g}^n, \mathbf{\Lambda} \right\rangle, \quad (3.6)$$

where $\langle \cdot, \cdot \rangle$ denotes an inner product and $\mathbf{\Lambda}$ is the Lagrange multiplier. Since in our previous work²²⁻²⁴ we have used a Finite Difference (FD) method for space discretization, we use the dot

product as the inner product and (3.6) becomes

$$\mathcal{L}(\mathbf{F}, \boldsymbol{\Lambda}, E) = \mathcal{J}^{n+1} + \mathcal{R}^{n+1}(E) + \left(\frac{\mathbf{F}}{\Delta t} - \rho^n \mathbf{b}(\mathbf{f}^n, E) - \mathbf{g}^n \right) \cdot \boldsymbol{\Lambda}. \quad (3.7)$$

If one were to use a different method for space discretization (e.g., a Finite Element method), a different inner product would be used (e.g., the L^2 inner product).

A saddle point of the Lagrangian functional can be identified among the stationary points. To find such stationary points, all the partial derivatives need to vanish:

$$\left. \frac{\partial \mathcal{L}}{\partial \boldsymbol{\Lambda}} \right|_{\mathbf{F}=\mathbf{f}^{n+1}} = \frac{\mathbf{f}^{n+1}}{\Delta t} - \rho^n \mathbf{b}(\mathbf{f}^n, \varepsilon^{n+1}) - \mathbf{g}^n = \mathbf{0}, \quad (3.8)$$

$$\left. \frac{\partial \mathcal{L}}{\partial \mathbf{F}} \right|_{\boldsymbol{\Lambda}=\boldsymbol{\lambda}^{n+1}} = \int_{\Omega} (\rho^{n+1} - \rho_v^{n+1}) \frac{\partial \rho^{n+1}}{\partial \mathbf{F}} [\mathbf{f}^{n+1}] d\mathbf{x} + \frac{\boldsymbol{\lambda}^{n+1}}{\Delta t} = \mathbf{0}, \quad (3.9)$$

$$\left. \frac{\partial \mathcal{L}}{\partial E} \right|_{E=\varepsilon^{n+1}} = \xi \int_{\Omega} (\varepsilon^{n+1} - \varepsilon_{ref}(\tau_{n+1}, \mathbf{x})) d\mathbf{x} - \rho^n \frac{\partial \mathbf{b}}{\partial E} [\varepsilon^{n+1}] \cdot \boldsymbol{\lambda}^{n+1} = 0. \quad (3.10)$$

Eq. (3.8) represents the state problem, eq. (3.9) the adjoint problem, and (3.10) is the optimality condition. So, at time t^{n+1} , we have the following coupled KKT system: find variable \mathbf{f}^{n+1} , Lagrange multiplier $\boldsymbol{\lambda}^{n+1}$, and parameter ε^{n+1} such that eq. (3.8)-(3.10) hold, with density ρ^{n+1} related to \mathbf{f}^{n+1} through (3.2). Note that the state problem (3.8) is exactly problem (3.1). If one chooses not to regularize the minimization of (3.3), which is equivalent to setting $\xi = 0$, the optimality condition (3.10) becomes a requirement of orthogonality for $\frac{\partial \mathbf{b}}{\partial E} [\varepsilon^{n+1}]$ and $\boldsymbol{\lambda}^{n+1}$.

4 Numerical solution of the inverse problem

A possible algorithm for the solution of coupled nonlinear system (3.8)-(3.10) is a steepest descent method. Let k denote the steepest descent method iteration. The algorithm reads as follows: at time t^{n+1} , iteration $k+1$, assuming that \mathbf{f}^n and ε_k are known, perform the following steps

- Step 1: Solve state problem

$$\frac{\mathbf{f}_{k+1}}{\Delta t} - \rho^n \mathbf{b}(\mathbf{f}^n, \varepsilon_k) = \mathbf{g}^n. \quad (4.1)$$

With \mathbf{f}_{k+1} , one reconstructs the approximation for the density ρ_{k+1} .

- Step 2: Solve adjoint problem

$$\frac{\boldsymbol{\lambda}_{k+1}}{\Delta t} = - \int_{\Omega} (\rho_{k+1} - \rho_v^{n+1}) \frac{\partial \rho_{k+1}}{\partial \mathbf{F}} [\mathbf{f}_{k+1}] d\mathbf{x}. \quad (4.2)$$

- Step 3: Given a suitable $\delta_{k+1} \in \mathbb{R}$, set

$$\varepsilon_{k+1} - \varepsilon_k = \delta_{k+1} \left(\xi \int_{\Omega} (\varepsilon_k - \varepsilon_{ref}(\tau_k, \mathbf{x})) d\mathbf{x} - \rho^n \frac{\partial \mathbf{b}}{\partial E}[\varepsilon_k] \cdot \boldsymbol{\lambda}_{k+1} \right). \quad (4.3)$$

- Step 4: Check stopping criterion

$$\frac{1}{|\Omega|} \left\| \xi \int_{\Omega} (\varepsilon_k - \varepsilon_{ref}(\tau_k, \mathbf{x})) d\mathbf{x} - \rho^n \frac{\partial \mathbf{b}}{\partial E}[\varepsilon_k] \cdot \boldsymbol{\lambda}_{k+1} \right\|_{L^2(\Omega)} < tol, \quad (4.4)$$

where tol is a given stopping tolerance. If satisfied, set $\mathbf{f}_h^{n+1} = \mathbf{f}_{k+1}$, $\rho_h^{n+1} = \rho_{k+1}$, and $\varepsilon^{n+1} = \varepsilon_{k+1}$. Otherwise, repeat steps 1 to 3.

4.1 Space discretization

For simplicity, we present space discretization using a rectangular computational $[0, L] \times [0, H]$, for given L and H . We generate a structured mesh of this domain by choosing Δx and Δy to partition interval $[0, L]$ and $[0, H]$, respectively. Let $N_x = L/\Delta x$ and $N_y = H/\Delta y$. We define the discrete mesh points $\mathbf{x}_{pq} = (x_p, y_q)$ by

$$\begin{aligned} x_p &= p\Delta x, & p &= 0, 1, \dots, N_x, \\ y_q &= q\Delta y, & q &= 0, 1, \dots, N_y. \end{aligned}$$

We also need to define:

$$\begin{aligned} x_{p+1/2} &= x_p + \Delta x/2 = \left(p + \frac{1}{2}\right)\Delta x, \\ y_{q+1/2} &= y_q + \Delta y/2 = \left(q + \frac{1}{2}\right)\Delta y. \end{aligned}$$

The space discretization of the state problem (4.1) is thoroughly described in Ref. 23. Here, we present the space discretization of the adjoint problem (4.2) and the update of the stress level from (4.3). Let us start from the problem (4.2).

Recalling that the density is computed from the probability functions through (3.2), it is easy to see that

$$\frac{\partial \rho_{k+1}}{\partial \mathbf{F}}[\mathbf{f}_{k+1}] = \mathbb{1}, \quad (4.5)$$

where $\mathbb{1} \in \mathbb{R}^{N_d}$ is a vector with all entries equal to 1. Then, we have

$$\frac{\lambda_{k+1}^i}{\Delta t} = - \int_{\Omega} (\rho_{k+1} - \rho_v^{n+1}) d\mathbf{x}, \quad i = 1, \dots, N_d, \quad (4.6)$$

i.e., all entries of $\boldsymbol{\lambda}_{k+1}$ are equal. This is due to the choice of an explicit time discretization scheme. If we were to, e.g., treat the convective in (2.10) implicitly, the components of $\boldsymbol{\lambda}_{k+1}$, which are associated to the different walking directions, would be different. The FD method we use produces an approximation of λ_{k+1}^i with cell average $\Lambda_{k+1}^{i,pq} \in \mathbb{R}$:

$$\Lambda_{k+1}^{i,pq} \approx \frac{1}{\Delta x \Delta y} \int_{y_{q-1/2}}^{y_{q+1/2}} \int_{x_{p-1/2}}^{x_{p+1/2}} \lambda_{k+1}^i(x, y) dx dy,$$

where $1 \leq p \leq N_x - 1$ and $1 \leq q \leq N_y - 1$. From (4.6), we get:

$$\Lambda_{k+1}^{i,pq} = -\Delta t \int_{y_{q-1/2}}^{y_{q+1/2}} \int_{x_{p-1/2}}^{x_{p+1/2}} (\rho_{k+1} - \rho_v^{n+1}) dx dy. \quad (4.7)$$

The FD approximation of λ_{k+1}^i , denoted by Λ_{k+1}^i , is given by a piece-wise constant function in space that takes value $\Lambda_{k+1}^{i,pq}$ over cell $[x_{p-1/2}, x_{p+1/2}] \times [y_{q-1/2}, y_{q+1/2}]$.

Now, let us take care of Step 3, which updates the value of the fear level. The FD approximation of eq. (4.3), using the same FD method used for (4.2) reads:

$$\begin{aligned} E_{k+1}^{pq} - E_k^{pq} = & \delta_{k+1} \zeta^{pq} \int_{y_{q-1/2}}^{y_{q+1/2}} \int_{x_{p-1/2}}^{x_{p+1/2}} (\varepsilon_k - \varepsilon_{ref}(\tau_k, \mathbf{x})) dx dy \\ & - \delta_{k+1} P^{n,pq} \frac{\partial \mathbf{b}^{pq}}{\partial E} [\varepsilon_k] \cdot \boldsymbol{\Lambda}_{k+1}^{pq}, \end{aligned} \quad (4.8)$$

where E_{k+1}^{pq} and E_k^{pq} are (subsequent) cell averages of ε_{k+1} and ε_k for the generic pq cell, $P^{n,pq}$ is the cell average of ρ^n , and $\boldsymbol{\Lambda}_{k+1}^{pq} \in \mathbb{R}^{N_d}$ is the vector whose generic i -th component is $\Lambda_{k+1}^{i,pq}$. Vector $\frac{\partial \mathbf{b}^{pq}}{\partial E} [\varepsilon_k]$ in (4.8) requires more explanation. Recall that $\mathbf{b}(\mathbf{f}^n, E) \in \mathbb{R}^{N_d}$ is the vector whose i -th entry is $(\mathbf{f}^n)^T \mathcal{B}^i(E) \mathbf{f}^n$, where $\mathcal{B}^i(E) \in \mathbb{R}^{N_d \times N_d}$ is the matrix whose hk entry is \mathcal{B}_{hk}^i defined in (2.8). So, the i -th entry of FD approximation of $\frac{\partial \mathbf{b}(\mathbf{f}^n, E)}{\partial E} [\varepsilon_k]$ is:

$$(\mathbf{F}^{n,pq})^T \frac{\partial \mathcal{B}^i}{\partial E} [\varepsilon_k] \mathbf{F}^{n,pq}, \quad (4.9)$$

where $\mathbf{F}^{n,pq}$ is the cell average of \mathbf{f}^n . From (2.9), it is easy to see that entry hk of matrix $\frac{\partial \mathcal{B}^i}{\partial E} [\varepsilon_k]$ is

$$\frac{\partial \mathcal{B}_{hk}^i}{\partial E} [\varepsilon_k] = \begin{cases} \frac{4}{\pi} \frac{1}{\sqrt{1 - (\mathbf{u}_P \cdot \mathbf{u}_i)^2}} \frac{\partial (\mathbf{u}_P \cdot \mathbf{u}_i)}{\partial E} [\varepsilon_k] & \text{if } |\arccos(\mathbf{u}_P \cdot \mathbf{u}_i)| \leq \frac{\pi}{4}, \\ 0 & \text{otherwise,} \end{cases} \quad (4.10)$$

with

$$\frac{\partial (\mathbf{u}_P \cdot \mathbf{u}_i)}{\partial E} [\varepsilon_k] = \frac{\varepsilon_k (\mathbf{u}_F \cdot \mathbf{u}_C - 1) (\mathbf{u}_F \cdot \mathbf{u}_i + \mathbf{u}_C \cdot \mathbf{u}_i) + \mathbf{u}_F \cdot \mathbf{u}_i - (\mathbf{u}_C \cdot \mathbf{u}_i) (\mathbf{u}_F \cdot \mathbf{u}_C)}{(-2\varepsilon_k^2 (\mathbf{u}_F \cdot \mathbf{u}_C) + 2\varepsilon_k \mathbf{u}_F \cdot \mathbf{u}_C + 2\varepsilon_k^2 - 2\varepsilon_k + 1)^{3/2}}.$$

5 Numerical results

The numerical experiments described in this section are inspired from the lab experiments on ants reported in Ref. 29, which were aimed at understanding the effects of structural features on collective movement patterns during rapid egress. Of the four scenarios studied in Ref. 29, we consider the following three:

- Ants escaping from a circular chamber without partial obstruction near exit in Sec. 5.1.
- Ants escaping from a circular chamber with partial obstruction (via a column) near exit is Sec. 5.2.
- Ants escaping from a square chamber with exit at the corner of the walls in Sec. 5.3.

The exit in each chamber is such that it allows unimpeded passage of a single ant or somewhat encumbered passage of two ants at the same time.

Several repetitions of these scenarios were performed by the authors of Ref. 29. In each experiment, the ants (numbering 200–250) were allowed to nest naturally in the chamber. Then, citronella (an insect repellent liquid) was injected through a small hole in the chamber ceiling to create panic. Upon the injection of the liquid, ants rushed to the exit in a manner reminiscent of humans in a crowd panic.

We start our simulations right after the citronella has been injected. Ref. 29 reports the mean time for the first 50 ants to escape the chamber. The data were obtained by manual counting from playback of digital video recordings. Our simulations try to match those averages by correcting the fear level through the optimization procedure described in Sec. 4.

As mentioned in Sec. 2.1, we work with nondimensional quantities. For this purpose, we need to define:

- a characteristic length D , which is the largest distance an active particle can cover in domain Ω ;
- a maximum moving speed V_M ;
- a reference time $T = D/V_M$;
- a maximum admissible number of active particles per unit area ρ_M .

For all the tests, we set $V_M = 2$ mm/s and $\rho_M = 0.5$ ants/mm², while the values of D and thus T vary depending on the geometry. For the circular chamber, we set $D = 35$ mm, while for the square chamber we take $D = 31\sqrt{2}$ mm. Then, the characteristic times are found by plugging the given D in $T = D/V_M$.

5.1 Circular chamber without partial obstruction near exit

The circular chamber has a diameter of 35 mm with one exit located in the middle of the right side. The exit size is 2.5 mm. See Fig. 5 (left). In this chamber, we introduce 200 ants. As shown in Fig. 2, ants tend to congregate in parts of the chamber, rather than being uniformly distributed in it. We initially distribute the 200 ants into two distinct groups: a circular group located towards the opposite end to the exit and a crescent-shaped group near the exit. See Fig. 5 (left). A similar distribution is observed in one of the experiments from Ref. 29, see Fig. 5 (right), where we also see the device used to inject the citronella. We assign initial moving direction θ_1 to the ants in the circular group and the opposite direction (i.e., θ_5) to the ants in the crescent-shaped group.

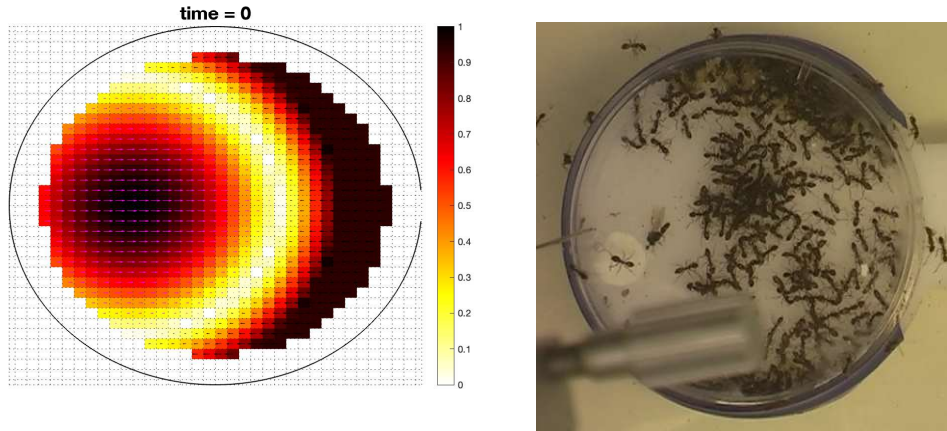


Figure 5: Left: Computational domain for the circular chamber without column, with initial density and direction for the numerical simulation. Right: snapshot from repetition 2 out of 30.

We chose the initial configuration described above because it leads to visibly different evacuation dynamics in conditions of low stress ($\varepsilon = 0.05$) vs high stress ($\varepsilon = 0.95$). See Fig. 6. We see that when the stress level is higher, regions of high density form around the center of the chamber at $t = 5, 10$ s. Additionally, at $t = 20$ the crowd density is high in an arrow-shaped region for $\varepsilon = 0.95$, while for $\varepsilon = 0.05$ the edge of the higher-density region is smoother.

For the numerical simulations in Fig. 6, we set $\Delta x = \Delta y = 1$ mm and $\Delta t = 0.5$ s. For the inverse problem, we will consider the computed results for $\varepsilon = 0.95$ as synthetic video data and start the optimization procedure described in Sec. 4 with $\varepsilon = 0.05$. We set $\delta_{k+1} = \delta = 50$ in (4.3) for all k , $tol = 1.0e - 05$ in (4.4), and choose not to use regularization. The comparison of synthetic data and optimized density is shown in Fig. 7, together with the corresponding optimized stress level. We see that the optimized density does not capture the high density regions around the center of the chamber at $t = 5, 10$ s, but does capture the arrow-shaped region at $t = 20$ s. Note that the optimized stress level does not vary from the initial value $\varepsilon = 0.05$ in the regions of the domain where the computed density matches the synthetic data, i.e., the low-density region

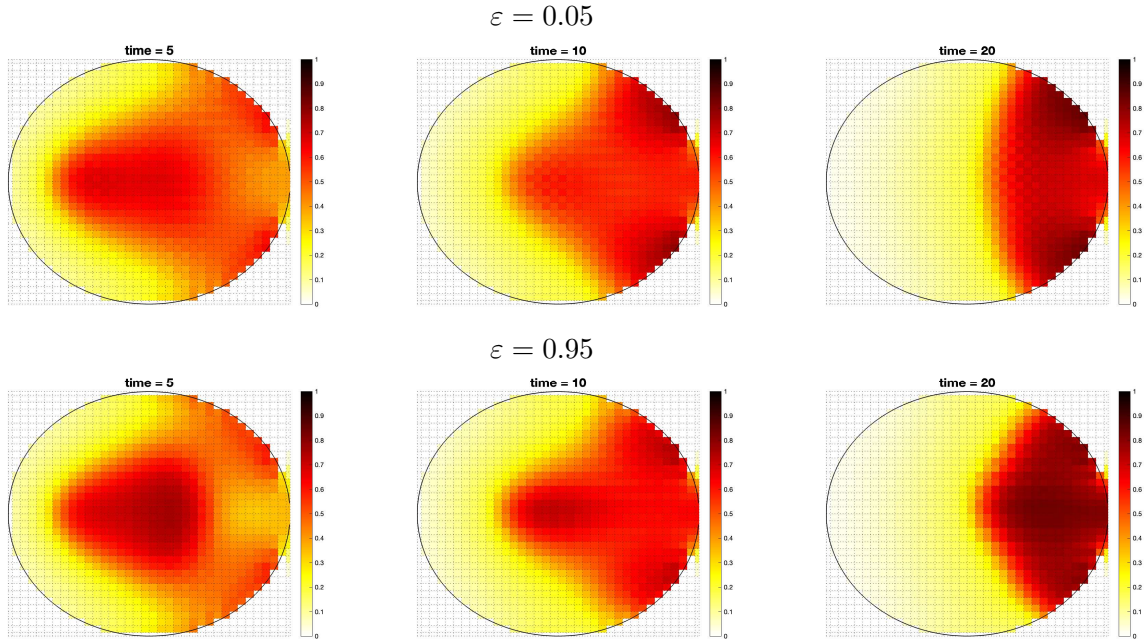


Figure 6: Computed density at $t = 5$ s (left), $t = 10$ s (center), and $t = 20$ s (right) given by the forward problem for 200 ants initially placed as in Fig. 5 (left) for $\varepsilon = 0.05$ (top row) and $\varepsilon = 0.95$ (second row).

in yellow, while it is increased where there is a mismatch, i.e., around the center of the chamber. However, while the procedure is correctly identifying where in the domain the fear level needs to be increased, the optimized value of the fear level is not large enough to match well the synthetic data around the center of the chamber.

Fig. 8 (left) shows the time evolution of functional (3.3), which quantifies the mismatch between synthetic density data and optimized density in the L^2 norm. Such mismatch is between 10^{-3} and $2.5 \cdot 10^{-3}$ for most of the first 20 s.

Fig. 8 (right) plots the number of ants inside the chamber over time. In 20 s, almost 50 ants have left the room. This is consistent with the findings from Ref. 29, where it is reported that the measured mean escape time (out of 30 repetitions) for the first 50 ants is 21.1 s (± 2 s standard deviation).

To improve upon the results presented in Fig. 7 and 8, we introduce regularization (3.4) with $\varepsilon_{ref} = 0.75$ and $\xi = 0.1$. The values of δ and tol remain unchanged. The comparison with the new optimized density is shown in Fig. 9. Thanks to the regularization term, the optimized density now correctly captures the high density regions around the center of the chamber at $t = 5, 10$ s, as well as the arrow-shaped region at $t = 20$ s. Note also the improved prediction of the number of ants in the chamber over time reported in Fig. 10 (right) with respect to Fig. 8 (right). By comparing

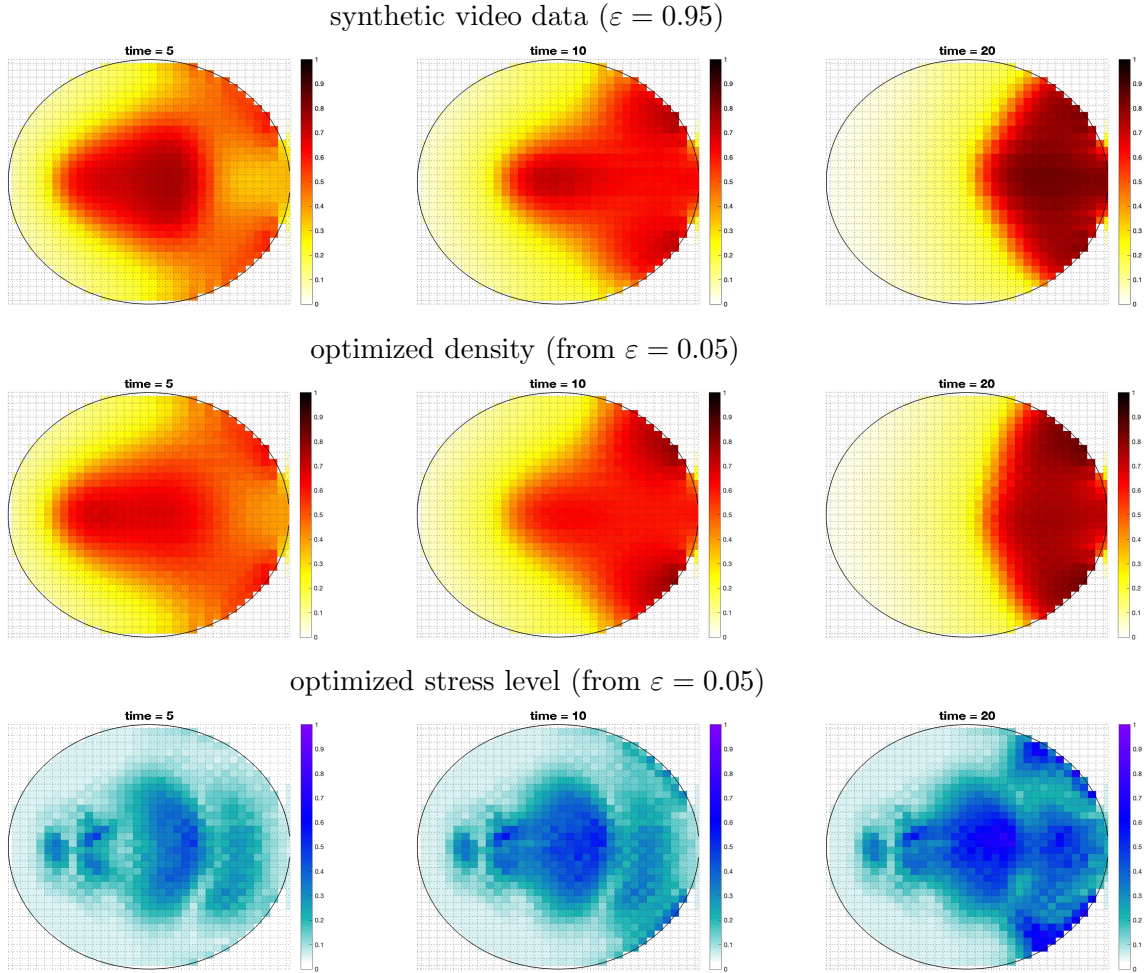


Figure 7: Synthetic density data (top), optimized density (center), optimized stress level (bottom) at $t = 5$ s (left), $t = 10$ s (center), and $t = 20$ s (right). Ants are initially placed as in Fig. 5 (left) and no regularization is used.

Fig. 10 (left) with Fig. 8 (left), we see that functional (3.5) takes smaller values than functional (3.3) for $t \geq 5$ s, which reflects the improved optimized density seen in Fig. 9 vs Fig. 7.

5.2 Circular chamber with partial obstruction

Let us consider the same circular chamber as in the previous section, but with the addition of a column to obstruct the exit. The column, which has a 5 mm diameter, is located 2 mm to the left of the exit, on the horizontal symmetry line. We place again 200 ants inside the chamber. The

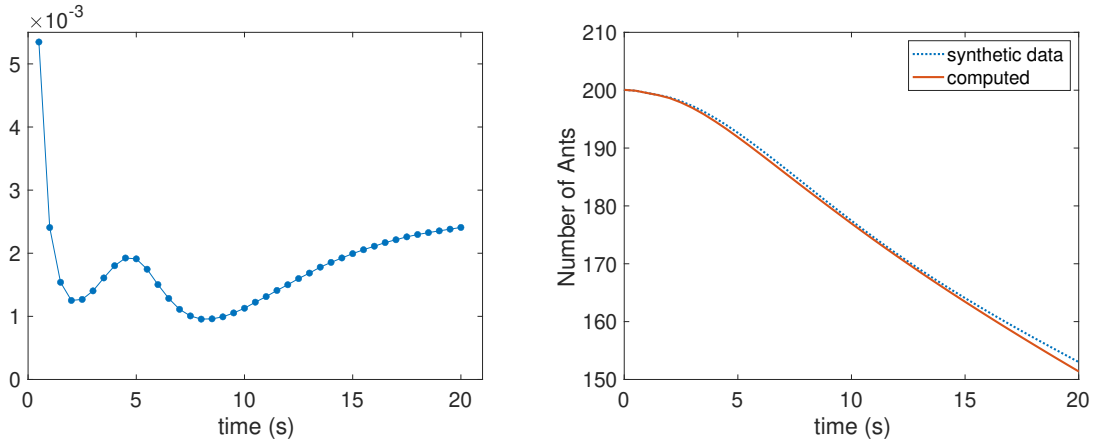


Figure 8: Left: Functional (3.3) over time for the circular chamber without column. Right: Number of ants inside the chamber over time.

initial density has a crescent-shaped high-density region. See Fig. 11 (left). A similar distribution is observed in one of the experiments from Ref. 29, see Fig. 11 (right). We assume all the ants initially move with direction θ_1 .

We consider again conditions of low stress ($\varepsilon = 0.05$) and high stress ($\varepsilon = 0.95$) in the initial configuration described above. The evacuation dynamics for the two cases are shown in Fig. 12. At $t = 5$ s, there is not significant difference between the computed densities for $\varepsilon = 0.05$ and $\varepsilon = 0.95$, but as time passes the high-density region becomes smaller and more uniform in space when the stress level is high. This is because the effect of the high stress is to make the active particles follow others, i.e., stick together instead of spreading out, as explained in Sec. 2.1.

We use same mesh size and time step as in the previous section, i.e., $\Delta x = \Delta y = 1$ mm and $\Delta t = 0.5$ s. We treat as synthetic video data the computed results for $\varepsilon = 0.95$ and start the optimization procedure with $\varepsilon = 0.05$. The values of δ and tol are also the same as in Sec. 5.1. However, for this second test case, we need to regularize the minimization problem to obtain results that match well the synthetic data. In particular, we choose regularization (3.4) with $\varepsilon_{ref} = 0.5$ and $\xi = 0.1$. The comparison of synthetic density data and optimized density is shown in Fig. 13, together with the corresponding optimized stress level. We observe that the synthetic data and the optimized density match well for the three times shown in Fig. 13. As for the optimized stress level, it remains close to the selected reference value ($\varepsilon_{ref} = 0.5$) over the low-density region, while it is slightly increased in the high-density region. This slight increase is sufficient for the optimized simulation to match the synthetic data.

To quantify the agreement seen in Sec. 13, Fig. 14 (left) shows the time evolution of functional (3.5). Aside from the first time few time steps, the value of functional (3.5) is of the order of 10^{-3} most of the time.

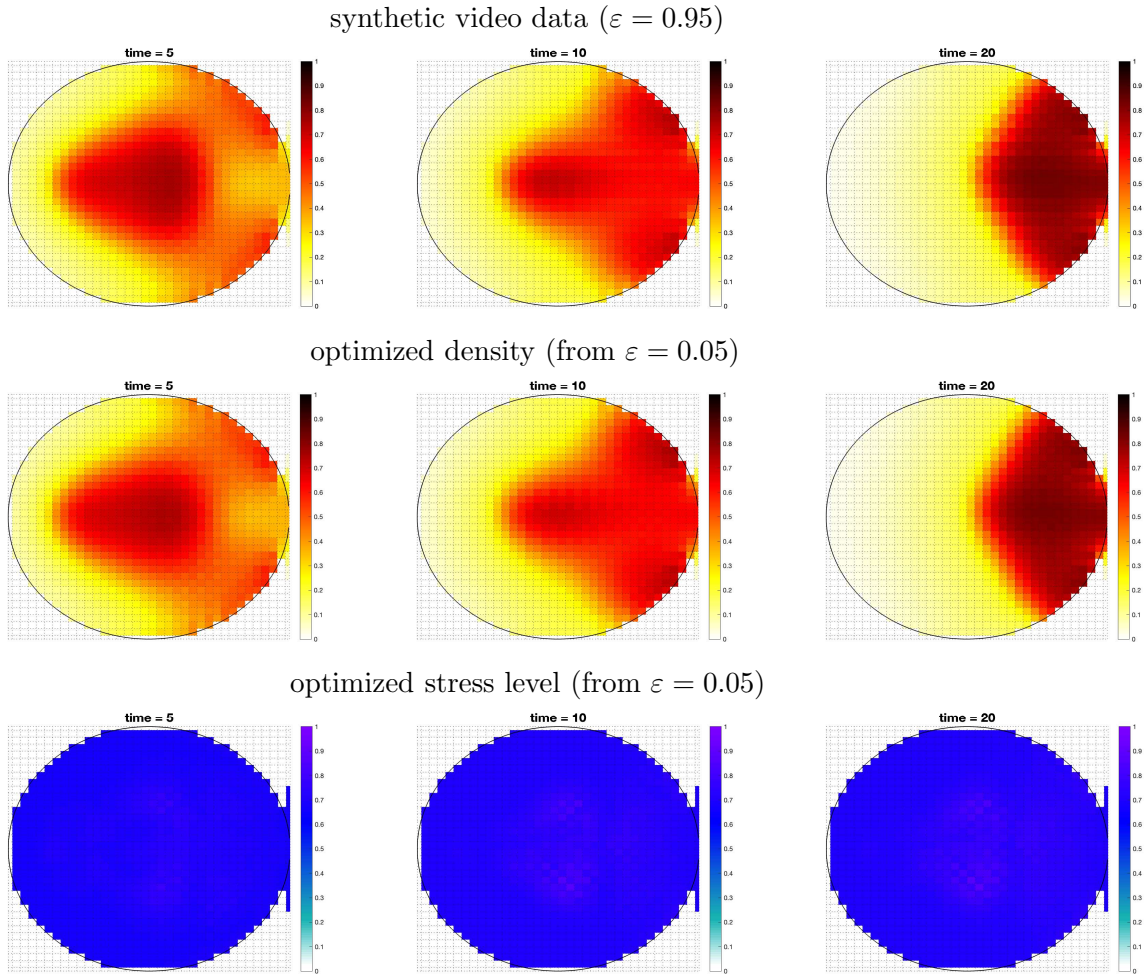


Figure 9: Synthetic density data (top), optimized density (center), optimized stress level (bottom) at $t = 5$ s (left), $t = 10$ s (center), and $t = 20$ s (right). Ants are initially placed as in Fig. 5 (left). The optimized results were obtained using regularization (3.4) with $\varepsilon_{ref} = 0.75$.

Fig. 14 (right) shows the number of ants inside the chamber over time. Although the computed densities in Fig. 13 agree with the synthetic data, we see that at $t = 20$ s there is a small difference in the number of ants left in the chamber according to the synthetic data (158) and the optimized results (155).

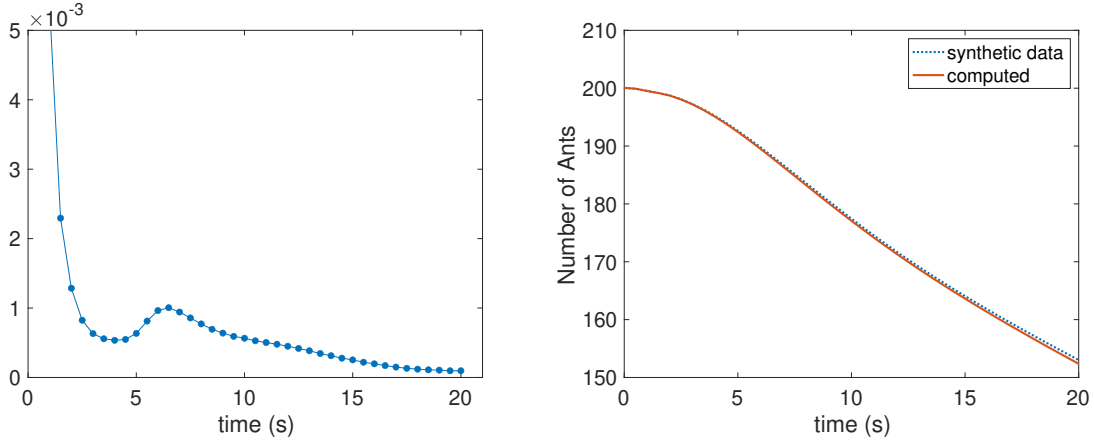


Figure 10: Left: Functional (3.5) over time for the circular chamber without column. Right: Number of ants inside the chamber over time.

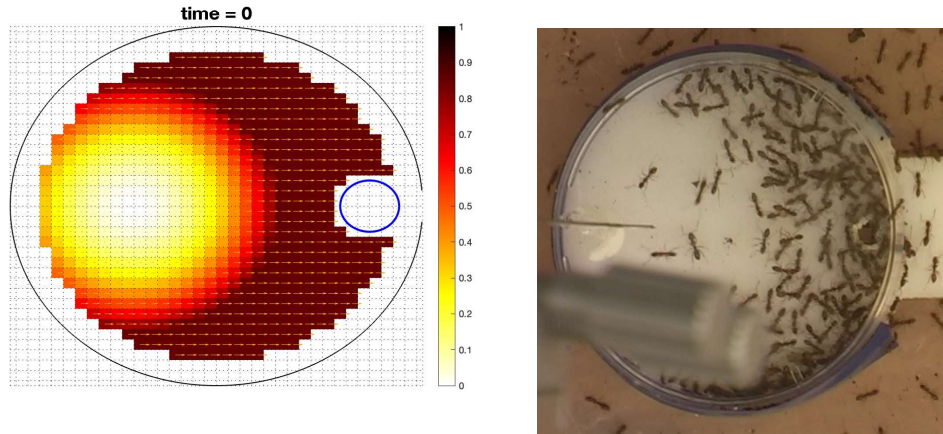


Figure 11: Left: Computational domain for the circular chamber with column, with initial density and direction for the numerical simulation. Right: snapshot from repetition 1 out of 30.

5.3 Square chamber with exit at the corner of the walls

The square chamber has a surface area equivalent to that of circular chamber, with the side measuring 31 mm. The exit is located at the upper right corner and it has size 2.5 mm. Like in the previous tests, we place 200 ants inside the chamber. We choose an initial distribution that mimics the one used in Sec. 5.1, i.e., a circular group and a crescent-shaped group. The initial moving direction was assigned as follows: we divided the square in quadrants and the ants in quadrant near the exit have initial direction θ_6 , while all others have initial direction θ_2 . See Fig. 15.

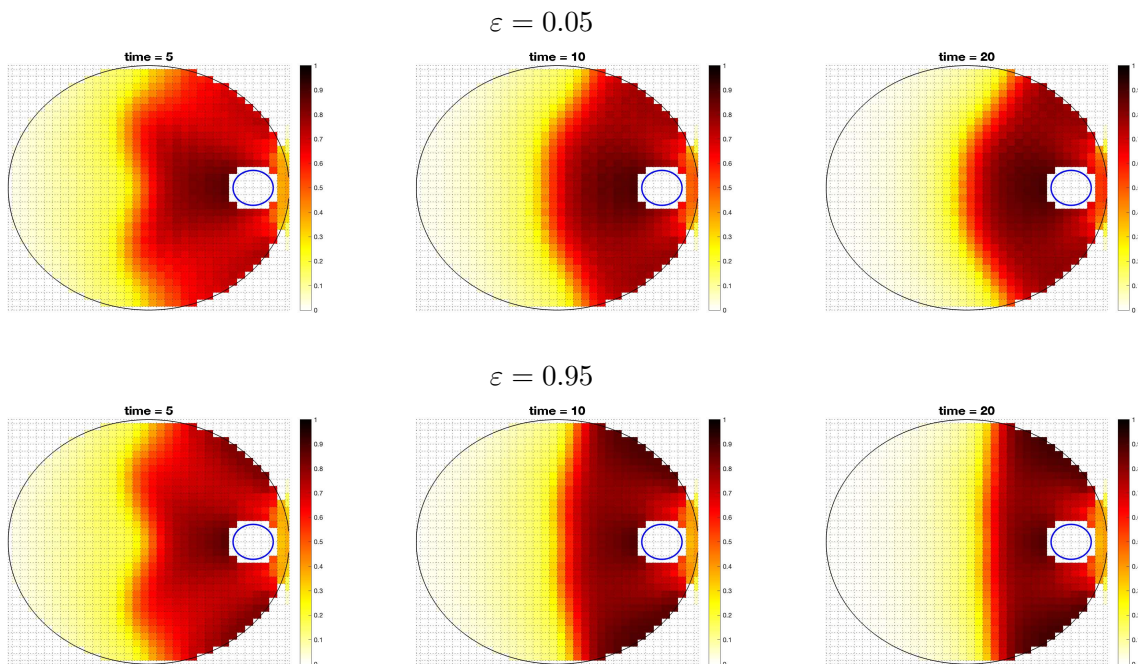


Figure 12: Computed density at $t = 5$ s (left), $t = 10$ s (center), and $t = 20$ s (right) given by the forward problem for 200 ants initially placed as in Fig. 11 (left) for $\varepsilon = 0.05$ (top row) and $\varepsilon = 0.95$ (second row).

The evacuation dynamics in conditions of low stress ($\varepsilon = 0.05$) and high stress ($\varepsilon = 0.95$) are shown in Fig. 16. Like in the case of the circular chamber with unobstructed exit in Sec. 5.1, we see that regions of high density form around the center of the chamber at $t = 5, 10$ s when the stress level is higher. At $t = 20$ s, the high-density region becomes smaller and more uniform in space when the stress level is $\varepsilon = 0.95$, which is similar to what observed in the circular chamber with partially obstructed exit in Sec. 5.2.

We use same mesh size and time step as in the previous sections, and treat as synthetic video data the computed results for $\varepsilon = 0.95$. The optimization procedure is started from $\varepsilon = 0.05$, with $\varepsilon_{ref} = 0.75$ and the same ξ , δ , and tol as in Sec. 5.2. The comparison of synthetic density data and optimized density is shown in Fig. 17, together with the corresponding optimized stress level. Thanks to the use of relaxation, the synthetic data and the optimized density match well. We see that the high-density regions around the center of the chamber at $t = 5, 10$ s are well captured. Similarly, the the high-density regions in the synthetic data and optimized density at $t = 20$ match well. The optimized stress level remains around the ε_{ref} value over most of the domain, but it has local peaks close to 0.95.

Fig. 18 (left) shows the time evolution of functional (3.5). Again, we see that the value of

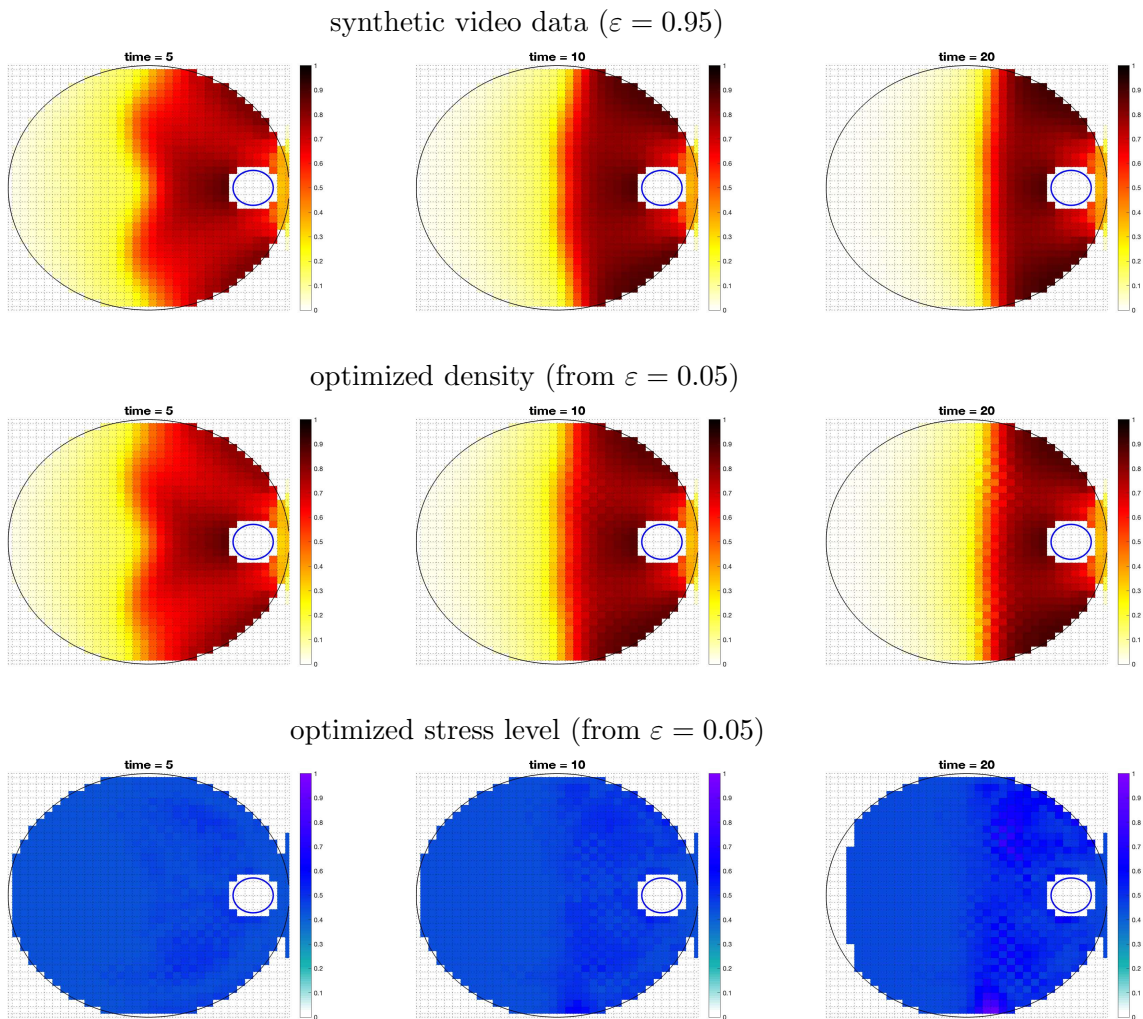


Figure 13: Synthetic density data (top), optimized density (center), optimized stress level (bottom) at $t = 5$ s (left), $t = 10$ s (center), and $t = 20$ s (right). Ants are initially placed as in Fig. 5 (left). The optimized results were obtained using regularization (3.4) with $\varepsilon_{ref} = 0.5$.

functional (3.5) is of the order of 10^{-3} most of the time.

Fig. 18 (right) shows the number of ants inside the chamber over time. The numbers of ants given by the synthetic data and the optimized simulation agree till about $t = 14$ s and then they grow slightly apart. From Fig. 18 (right), we see that it takes about 12.5 s for the first 50 ants to leave the room. This is also consistent with the measured mean escape time (out of 10 repetitions in Ref. 29) for the first 50 ants, which is $12.9 \text{ s} \pm 0.5 \text{ s}$ standard deviation.

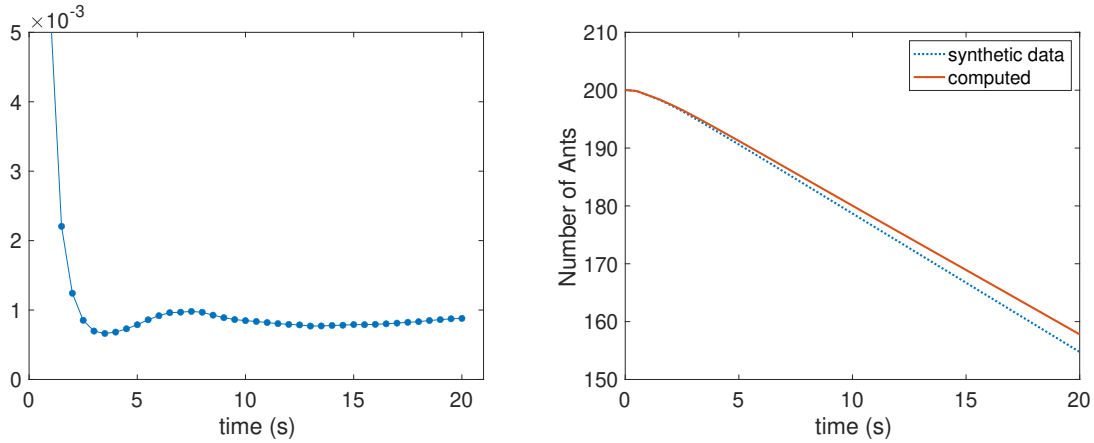


Figure 14: Left: Functional (3.5) over time for the circular chamber with column. Right: Number of ants inside the chamber over time.

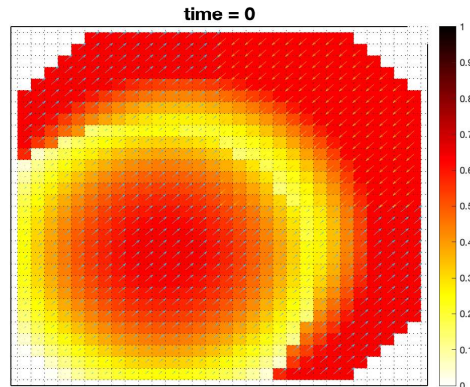


Figure 15: Computational domain for the square chamber with exit at the corner of the walls (top right).

6 Conclusions and perspectives

The large majority of existing mathematical models for crowd dynamics assume that pedestrians do not alter their, typically rational, walking behavior during the time interval of interest. Such models cannot be used to simulate emergency situations, like forced evacuations, when people may behave irrationally in response to fear. In this paper, we consider a kinetic model for crowd dynamics that features a parameter representing the stress level and we present a data-driven technique to set this parameter.

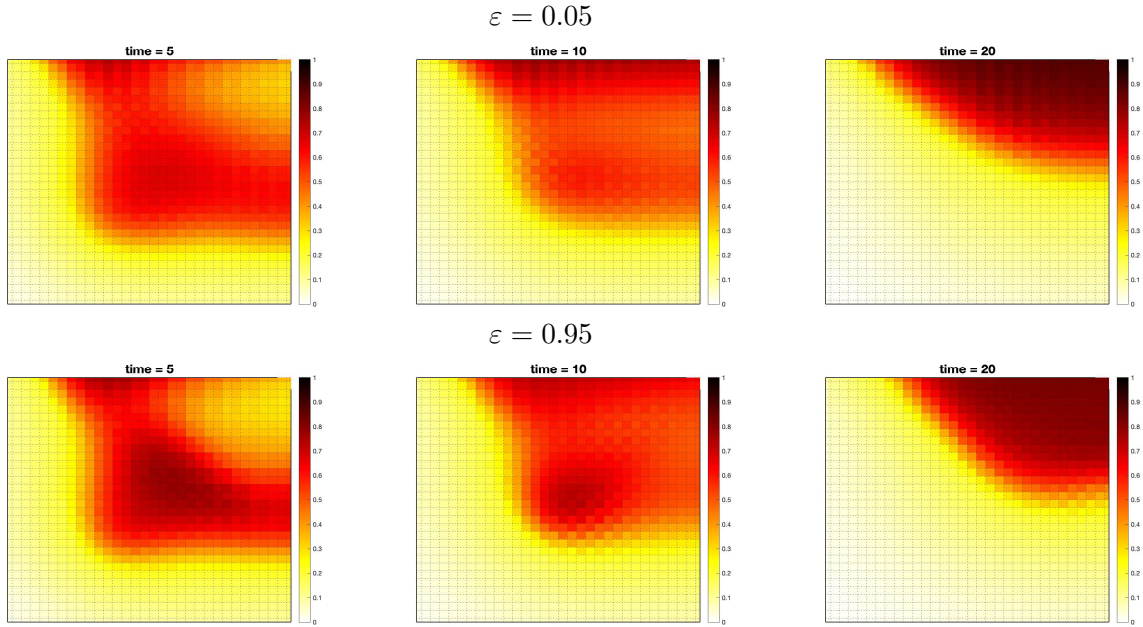


Figure 16: Computed density at $t = 5$ s (left), $t = 10$ s (center), and $t = 20$ s (right) given by the forward problem for 200 ants initially placed as in Fig. 15 for $\varepsilon = 0.05$ (top row) and $\varepsilon = 0.95$ (second row).

The data-driven technique is a minimization approach, based on an inverse crowd dynamics problem and a suitable functional measuring the distance between given crowd density data and the numerical solution. We applied this new methodology to model problems inspired from the experiments on panicked ants in Ref. 29, with synthetic data generated by numerical simulations of the forward problem. Our numerical experiments indicate that regularization is needed to obtain computed results that match well the density data. We used a regularization term that requires a reference value for the stress level parameter, i.e., one needs a good guess for the stress level in order for the proposed approach to yield accurate results.

The next step is to apply our methodology with the data extracted from the video recordings of the experiments in Ref. 29 and further investigate the sensitivity to the reference stress level.

Acknowledgments

We thank Dr. Martin Burd (Monash University) and Dr. Nirajan Shiwakoti (RMIT University) for sharing with us the video recordings of their experiments on ants in the circular chamber with and without partial obstruction near the exit. D.L. acknowledges support of Simons Foundation grant MPS-TSM-00002738.

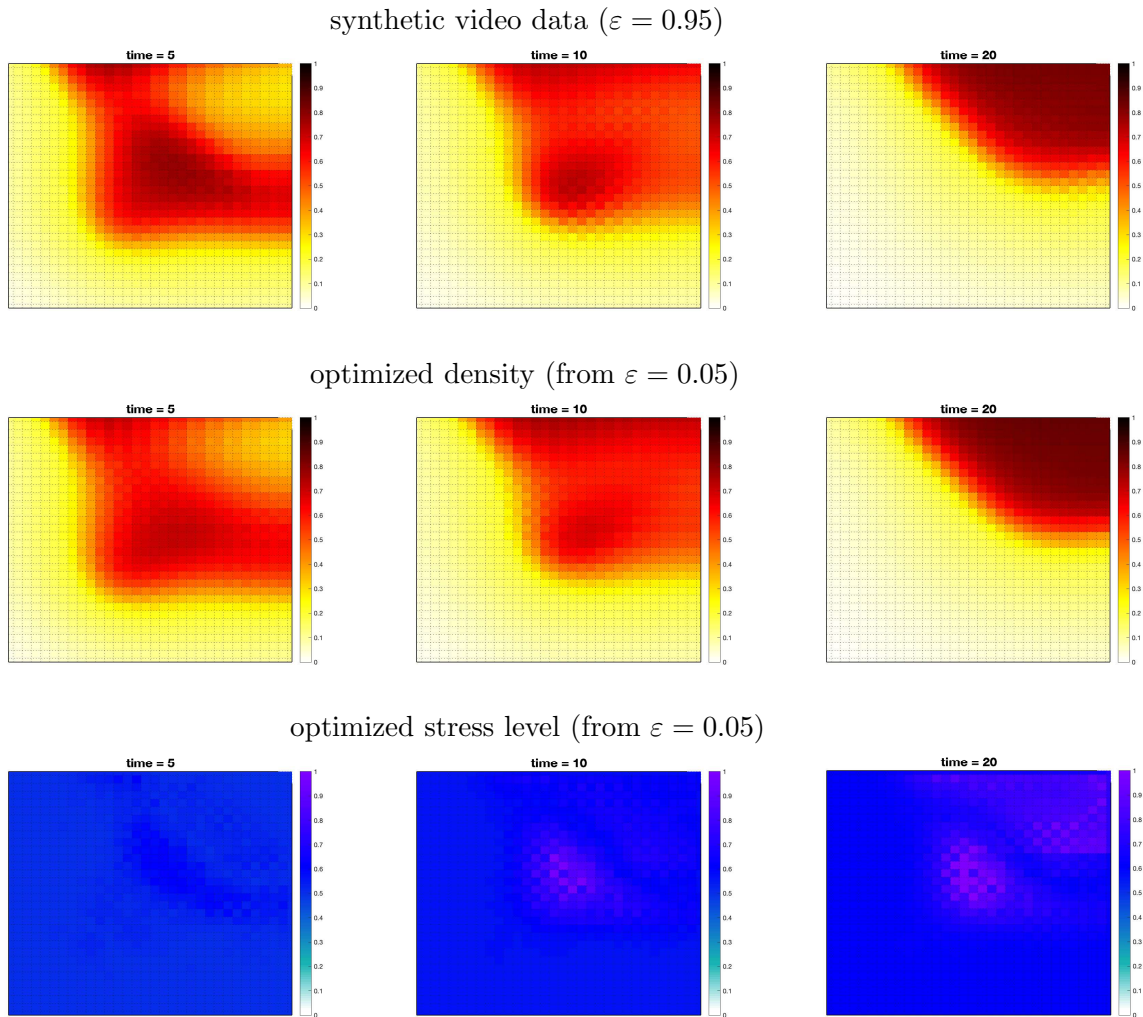


Figure 17: Synthetic density data (top), optimized density (center), optimized stress level (bottom) at $t = 5$ s (left), $t = 10$ s (center), and $t = 20$ s (right). Ants are initially placed as in Fig. 15. The optimized results were obtained using regularization (3.4) with $\varepsilon_{ref} = 0.75$.

References

- ¹ J. P. Agnelli, F. Colasuonno, and D. Knopoff. A kinetic theory approach to the dynamics of crowd evacuation from bounded domains. *Mathematical Models and Methods in Applied Sciences*, 25(01):109–129, 2015.
- ² V.V. Aristov. Biological systems as nonequilibrium structures described by kinetic methods.

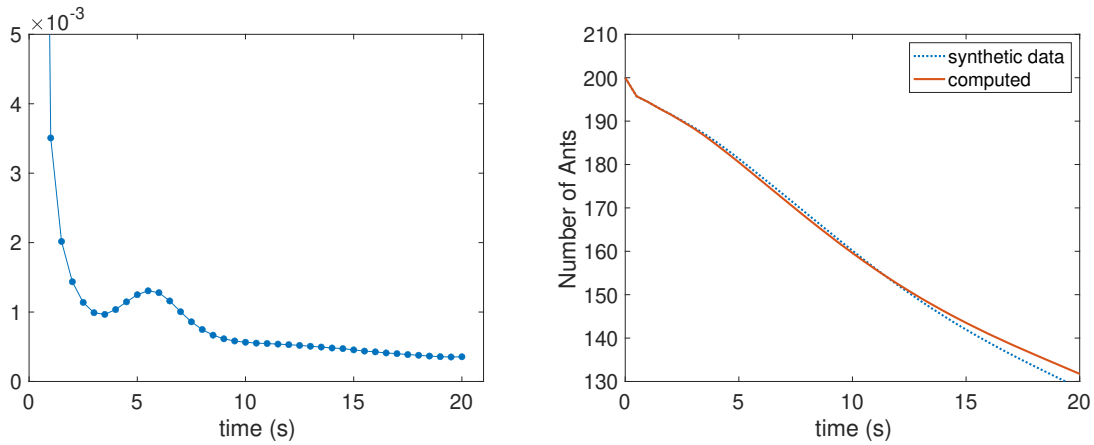


Figure 18: Left: Functional (3.5) over time for the square chamber. Right: Number of ants inside the chamber over time.

Results in Physics, 13:102232, 2019.

³ M. K. Banda, M. Herty, and T. Trimborn. *Recent Developments in Controlled Crowd Dynamics*, pages 133–157. Springer International Publishing, Cham, 2020.

⁴ N. Bellomo and A. Bellouquid. On multiscale models of pedestrian crowds from mesoscopic to macroscopic. *Communications in Mathematical Sciences*, 13:1649–1664, 2015.

⁵ N. Bellomo, A. Bellouquid, L. Gibelli, and N. Outada. *A quest towards a mathematical theory of living systems*. Modeling and Simulation in Science, Engineering and Technology. (Birkhäuser, 2017), 2017.

⁶ N. Bellomo, A. Bellouquid, and D. Knopoff. From the microscale to collective crowd dynamics. *SIAM Multiscale Modeling & Simulation*, 11(3):943–963, 2013.

⁷ N. Bellomo, D. Clarke, L. Gibelli, P. Townsend, and B.J. Vreugdenhil. Human behaviours in evacuation crowd dynamics: From modelling to “big data” toward crisis management. *Physics of Life Reviews*, 18:1–21, 2016.

⁸ N. Bellomo and L. Gibelli. Toward a mathematical theory of behavioral-social dynamics for pedestrian crowds. *Mathematical Models and Methods in Applied Sciences*, 25(13):2417–2437, 2015.

⁹ N. Bellomo, L. Gibelli, and N. Outada. On the interplay between behavioral dynamics and social interactions in human crowds. *Kinetic and Related Models*, 12(2):397–409, 2019.

- ¹⁰ Nicola Bellomo, Marina Dolfin, and Jie Liao. Life and self-organization on the way to artificial intelligence for collective dynamics. *Physics of Life Reviews*, 51:1–8, 2024.
- ¹¹ Nicola Bellomo, Livio Gibelli, Annalisa Quaini, and Alessandro Reali. Towards a mathematical theory of behavioral human crowds. *Mathematical Models and Methods in Applied Sciences*, 32(02):321–358, 2022.
- ¹² Nicola Bellomo, Jie Liao, Annalisa Quaini, Lucia Russo, and Constantinos Siettos. Human behavioral crowds review, critical analysis and research perspectives. *Mathematical Models and Methods in Applied Sciences*, 33(08):1611–1659, 2023.
- ¹³ Aniket Bera, Sujeong Kim, and Dinesh Manocha. Online parameter learning for data-driven crowd simulation and content generation. *Computers & Graphics*, 55:68–79, 2016.
- ¹⁴ Andrea L. Bertozzi, Jesús Rosado, Martin B. Short, and Li Wang. Contagion shocks in one dimension. *Journal Statistical Physics*, 158:647–664, 2015.
- ¹⁵ Yuehai Chen, Jing Yang, Badong Chen, and Shaoyi Du. Counting varying density crowds through density guided adaptive selection cnn and transformer estimation. *IEEE Transactions on Circuits and Systems for Video Technology*, 33(3):1055–1068, 2022.
- ¹⁶ Min Fu, Pei Xu, Xudong Li, Qihe Liu, Mao Ye, and Ce Zhu. Fast crowd density estimation with convolutional neural networks. *Engineering Applications of Artificial Intelligence*, 43:81–88, 2015.
- ¹⁷ Milad Haghani and Majid Sarvi. Social dynamics in emergency evacuations: Disentangling crowd’s attraction and repulsion effects. *Physica A: Statistical Mechanics and its Applications*, 475:24–34, 2017.
- ¹⁸ D. Helbing, I. Farkas, and T. Vicsek. Simulating dynamical features of escape panic. *Natures*, 407:487–490, 2000.
- ¹⁹ Dirk Helbing and Anders Johansson. *Pedestrian, Crowd, and Evacuation Dynamics*, pages 1–28. Springer New York, New York, NY, 2009.
- ²⁰ Dirk Helbing, Anders Johansson, and Habib Zein Al-Abideen. Dynamics of crowd disasters: An empirical study. *Phys. Rev. E*, 75:046109, Apr 2007.
- ²¹ Muhammad Asif Khan, Hamid Menouar, and Ridha Hamila. Revisiting crowd counting: State-of-the-art, trends, and future perspectives. *Image and Vision Computing*, 129:104597, 2023.
- ²² D. Kim, K. O’Connell, W. Ott, and A. Quaini. A kinetic theory approach for 2D crowd dynamics with emotional contagion. *Mathematical Models and Methods in Applied Sciences, Accepted.*, 31(6):1137–1162, 2021.

- ²³ D. Kim and A. Quaini. A kinetic theory approach to model pedestrian dynamics in bounded domains with obstacles. *Kinetic & Related Models*, 12(6):1273–1296, 2019.
- ²⁴ D. Kim and A. Quaini. Coupling kinetic theory approaches for pedestrian dynamics and disease contagion in a confined environment. *Mathematical Models and Methods in Applied Sciences*, 30(10):1893–1915, 2020.
- ²⁵ Kang Hoon Lee, Myung Geol Choi, Qyoun Hong, and Jehee Lee. Group behavior from video: a data-driven approach to crowd simulation. In *Proceedings of the 2007 ACM SIG-GRAPH/Eurographics Symposium on Computer Animation*, SCA '07, page 109–118, Goslar, DEU, 2007. Eurographics Association.
- ²⁶ A NSAV Marana, Sergio A Velastin, L da F Costa, and RA Lotufo. Automatic estimation of crowd density using texture. *Safety Science*, 28(3):165–175, 1998.
- ²⁷ Yalda Rahmati and Alireza Talebpour. Learning-based game theoretical framework for modeling pedestrian motion. *Phys. Rev. E*, 98:032312, Sep 2018.
- ²⁸ A. Schadschneider and A. Seyfried. Empirical results for pedestrian dynamics and their implications for modeling. *Networks and Heterogeneous Media*, 6(3):545–560, 2011.
- ²⁹ Nirajan Shiwakoti, Majid Sarvi, Geoff Rose, and Martin Burd. Animal dynamics based approach for modeling pedestrian crowd egress under panic conditions. *Transportation Research Part B: Methodological*, 45(9):1433–1449, 2011. Select Papers from the 19th ISTTT.
- ³⁰ Jinhuan Wang, Lei Zhang, Qiongyu Shi, Peng Yang, and Xiaoming Hu. Modeling and simulation for congestion pedestrian evacuation with panic. *Physica A: Statistical Mechanics and its Applications*, 428:396–409, 2015.
- ³¹ L. Wang, M. B. Short, and A. L. Bertozzi. Efficient numerical methods for multiscale crowd dynamics with emotional contagion. *Mathematical Models and Methods in Applied Sciences*, 27(1):205–230, 2017.
- ³² Nanda Wijermans, Claudine Conrado, Maarten van Steen, Claudio Martella, and Jie Li. A landscape of crowd-management support: An integrative approach. *Safety Science*, 86:142–164, 2016.
- ³³ Mingliang Xu, Xiaozheng Xie, Pei Lv, Jianwei Niu, Hua Wang, Chaochao Li, Ruijie Zhu, Zhigang Deng, and Bing Zhou. Crowd behavior simulation with emotional contagion in unexpected multi-hazard situations. *IEEE Transactions on Systems, Man, and Cybernetics: Systems*, 51(3):1567–1581, 2021.
- ³⁴ Zhenzhen Yao, Guijuan Zhang, Dianjie Lu, and Hong Liu. Data-driven crowd evacuation: A reinforcement learning method. *Neurocomputing*, 366:314–327, 2019.

³⁵ Y. Zou, J. Xie, and B. Wang. Evacuation of pedestrians with two motion modes for panic system. *PLoS ONE*, 11(4):e0153388, 2016.